Cytoglobin has potent superoxide dismutase function

Jay L. Zweier[a,b,1], Craig Hemann[a,b], Tapan Kundu[a,b], Mohamed G. Ewees[a,b], Sahar A. Khaleel[a,b,2], Alexandre Samouilov[a,b], Govindasamy Ilangovan[a,b], and Mohamed A. El-Mahdy[a,b]

[a]Department of Internal Medicine, Division of Cardiovascular Medicine, The Ohio State University, Columbus, OH 43210; and [b]Davis Heart and Lung Research Institute, College of Medicine, The Ohio State University, Columbus, OH 43210

Edited by Mark Gladwin, University of Pittsburgh, Pittsburgh, PA; received for review March 15, 2021; accepted October 21, 2021, by Editorial Board Member Carl F. Nathan

Cytoglobin (Cygb) was discovered as a novel type of globin that is expressed in mammals; however, its functions remain uncertain. While Cygb protects against oxidant stress, the basis for this is unclear, and the effect of Cygb on superoxide metabolism is unknown. From dose-dependent studies of the effect of Cygb on superoxide catabolism, we identify that Cygb has potent superoxide dismutase (SOD) function. Initial assays using cytochrome *c* showed that Cygb exhibits a high rate of superoxide dismutation on the order of 10^8 $M^{-1} \cdot s^{-1}$. Spin-trapping studies also demonstrated that the rate of Cygb-mediated superoxide dismutation (1.6×10^8 $M^{-1} \cdot s^{-1}$) was only ∼10-fold less than Cu,Zn-SOD. Stopped-flow experiments confirmed that Cygb rapidly dismutates superoxide with rates within an order of magnitude of Cu,Zn-SOD or Mn-SOD. The SOD function of Cygb was inhibited by cyanide and CO that coordinate to Fe^{3+}-Cygb and Fe^{2+}-Cygb, respectively, suggesting that dismutation involves iron redox cycling, and this was confirmed by spectrophotometric titrations. In control smooth-muscle cells and cells with siRNA-mediated Cygb knockdown subjected to extracellular superoxide stress from xanthine/xanthine oxidase or intracellular superoxide stress triggered by the uncoupler, menadione, Cygb had a prominent role in superoxide metabolism and protected against superoxide-mediated death. Similar experiments in vessels showed higher levels of superoxide in *Cygb*$^{-/-}$ mice than wild type. Thus, Cygb has potent SOD function and can rapidly dismutate superoxide in cells, conferring protection against oxidant injury. In view of its ubiquitous cellular expression at micromolar concentrations in smooth-muscle and other cells, Cygb can play an important role in cellular superoxide metabolism.

superoxide | SOD | ROS | EPR | free radical

Over the last decade, cytoglobin (Cygb) was discovered as a fourth globin type expressed in mammals, predominantly in fibroblasts, smooth muscle, and related cell types in different organs and tissues (1–3). Since Cygb has structural similarity to myoglobin (Mb) and hemoglobin (Hb) and is up-regulated in tissues upon hypoxia (4), it has been suggested that Cygb may play a role in storing O_2, facilitating O_2 diffusion and sensing, NO dioxygenation, or protecting against oxidative stress (1, 4–6). The Cygb concentration in cells is ∼1 to 5 μM (5–7), which is much less than Hb concentration in red blood cells (∼8 mM) and Mb in cardiac and striated muscle (hundreds of micromolar to millimolar), resulting in a much lower capacity for O_2 storage or ability to facilitate O_2 diffusion. Thus, major questions remain about the function of Cygb and why there is a need for this additional globin.

There is an emerging body of evidence which suggests that Cygb may provide protection from oxidative cellular injury, possibly due to its ability to scavenge or catabolize reactive oxygen species (ROS) (8–10). Overexpression of Cygb has been shown to decrease the levels of chemically induced ROS and to provide protection from pro-oxidant injury. Conversely, down-regulation of Cygb sensitizes cells to the damaging effects of oxidant exposure and to oxidative DNA damage (8–10). Cells and organs lacking Cygb are more prone to radiation-induced injury as well as fibrosis and inflammatory disease (8).

While Cygb is reported to protect against oxidative stress, the mechanistic basis for this antioxidative efficacy has remained unclear. To date, the precise effect of Cygb on superoxide ($O_2^{\bullet-}$) metabolism is unknown. We hypothesize that Cygb can function to degrade $O_2^{\bullet-}$ and is a potent superoxide dismutase (SOD). Therefore, we perform studies to determine the dose-dependent effect of Cygb on the $O_2^{\bullet-}$ generated from xanthine (X) and xanthine oxidase (XO).

We demonstrate that Cygb has potent SOD function. The rate of its $O_2^{\bullet-}$ dismutation measured from the concentration-dependent reaction with cytochrome *c* (cyt *c*) or the spin trap 5-(diisopropoxy-phosphoryl)-5-methyl-1-pyrroline-*N*-oxide (DIPPMPO) or direct stopped-flow measurements is determined to be within an order of magnitude of that of copper-zinc SOD (Cu,Zn-SOD) and manganese SOD (Mn-SOD). In smooth muscle cells (SMCs) subjected to oxidative stress, we also show that Cygb plays a major role in the metabolism of $O_2^{\bullet-}$ and protects the cells against $O_2^{\bullet-}$-mediated death.

Significance

We identified a novel function of cytoglobin (Cygb) as an efficient superoxide dismutase (SOD) with a high–bimolecular dismutation rate on the order of 10^8 $M^{-1} \cdot s^{-1}$. It is the first Fe-centered SOD identified in mammalian cells and the only member of the globin family shown to have potent SOD activity. This SOD function of Cygb may serve to explain the prior reports of its antioxidative activity and the toxicities and disease seen with its genetic deletion, including the increased incidence of tumors. Combined with its potent NO dioxygenase activity, Cygb would be highly effective in decreasing both $O_2^{\bullet-}$ and NO levels, serving to decrease the formation of peroxynitrite and secondary oxidative injury.

Author contributions: J.L.Z. designed research; C.H., T.K., M.G.E., S.A.K., and M.A.E. performed research; J.L.Z., C.H., and T.K. contributed new reagents/analytic tools; J.L.Z., C.H., T.K., M.G.E., S.A.K., A.S., G.I., and M.A.E. analyzed data; and J.L.Z., C.H., T.K., A.S., G.I., and M.A.E. wrote the paper.

The authors declare no competing interest.

This article is a PNAS Direct Submission. M.G. is a guest editor invited by the Editorial Board.

[1]To whom correspondence may be addressed. Email: Jay.Zweier@osumc.edu.

[2]Present address: Department of Pharmacology & Toxicology, College of Pharmacy for Girls, Al-Azhar University, Cairo, Egypt.

This article contains supporting information online at http://www.pnas.org/lookup/suppl/doi:10.1073/pnas.2105053118/-/DCSupplemental.

Published December 20, 2021.

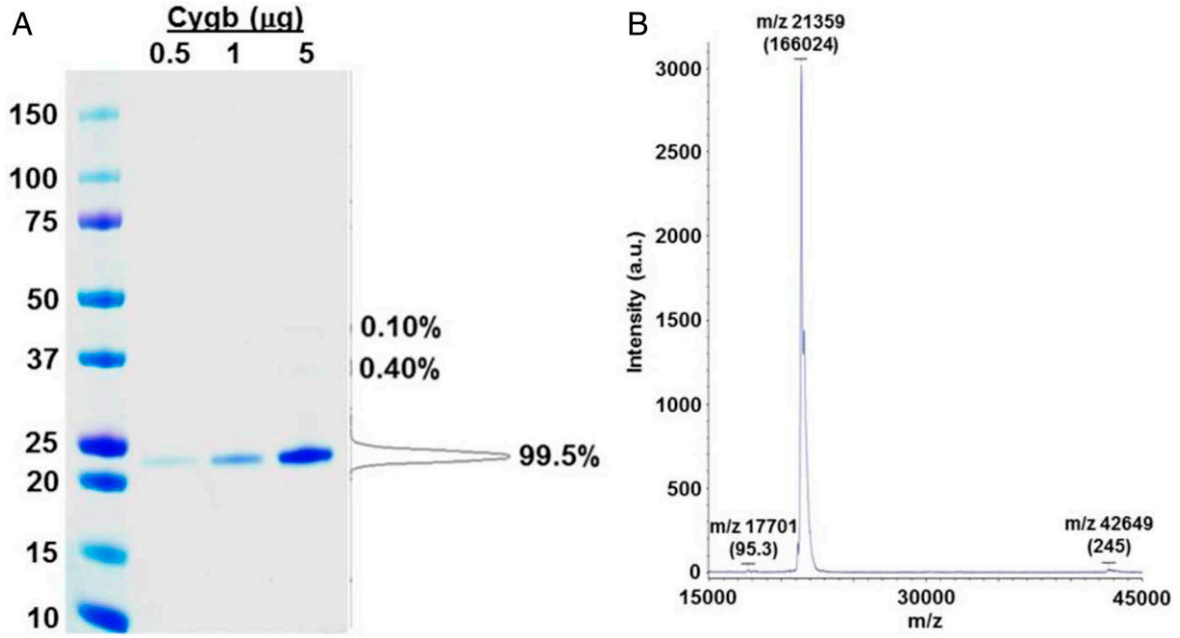

Fig. 1. Measurement of the purity of Cygb by SDS PAGE and MALDI-TOF MS. (*A*) The gel lanes are the following: Lane 1: Molecular weight markers, Lane 2: 0.5 μg Cygb, Lane 3: 1.0 μg Cygb, and Lane 4: 5.0 μg Cygb. Densitometry of the 5 μg lane of the gel is shown on the right. Cygb accounts for >99% of the total density of that gel lane. (*B*) MALDI-TOF MS data showing the Cygb peak at ~21.4 kDa with very high purity. Peaks are labeled by mass with the peak areas in parenthesis.

Results

Purity of Cygb Preparations. Recombinant human Cygb (rh-Cygb) was prepared and purified to high purity. On SDS PAGE (polyacrylamide gel electrophoresis), only a single band was seen with a molecular weight of ~21.4 kDa. Based on this, its purity was estimated to be >98% (Fig. 1). To further determine the purity of the Cygb preparation, mass spectroscopy (MS) studies were performed using matrix assisted laser desorption ionization–time of flight MS (MALDI TOF), in which it was confirmed that >98% purity was obtained. Since *Escherichia coli* has SOD isoforms with molecular weight (MW) close to that of Cygb, including a Fe-SOD, SOD B with MW of 21,310 Da, and a Mn-SOD, SOD A with MW 23,083 Da, additional studies were performed to further confirm the absence of any significant contamination by other SODs. The protein was subjected to trypsin digestion and tandem MS (MS/MS) performed on a sensitive Fusion MS/MS instrument. It was determined that there was ≤0.04% *E. coli* SOD B and <0.01% SOD A or SOD C. Thus, the Cygb was shown to be highly pure with no significant contamination with any *E. coli* or other known SOD.

Cyt *c* Measurements of SOD Function. For initial evaluation of the $O_2^{\bullet-}$ scavenging efficiency of Cygb, the cyt *c* reduction assay was performed whereby ferric cyt *c* is reduced by $O_2^{\bullet-}$ to ferrous cyt *c*. The X/XO $O_2^{\bullet-}$ generating system was used in the presence of a wide range of Cygb concentrations. In order to compare the $O_2^{\bullet-}$ scavenging efficiency to Cu,Zn-SOD, inhibition measurements were also performed as a function of Cu,Zn-SOD concentration. From the linear portion of the curves (up to 30 s), the initial rates of cyt *c* reduction were determined in the absence (V_0) or in the presence (V_i) of various concentrations of either Cygb or Cu,Zn-SOD. The ratios (V_i/V_0) of the rates of cyt *c* reduction versus the concentrations of Cygb or Cu,Zn-SOD (labeled SOD1 in the figures) were plotted and fitted with nonlinear regression (Fig. 2). Amounts of Cygb and Cu,Zn-SOD required for 50% inhibition of rates of $O_2^{\bullet-}$-mediated cyt *c* reduction were then derived from the hyperbolic fit to the data and are found to be 87.2 ± 8.8 nM and 11.0 ± 0.2 nM, respectively. Therefore, 87.2 nM of Cygb or 11.0 nM of Cu,Zn-SOD competes equally with 5×10^{-5} M cyt *c* for the $O_2^{\bullet-}$. Assuming the bimolecular rate constant for the reaction between $O_2^{\bullet-}$ and cyt *c* as 2.6×10^5 $M^{-1} \cdot s^{-1}$ (11), the second-order rate constants for the enzymatic dismutation of $O_2^{\bullet-}$ by Cygb and Cu,Zn-SOD were estimated to be $(1.52 \pm 0.15) \times 10^8$ $M^{-1} \cdot s^{-1}$ and $(1.20 \pm 0.03) \times 10^9$ $M^{-1} \cdot s^{-1}$, respectively. The rate constant determined for the dismutation of $O_2^{\bullet-}$ by Cu,Zn-SOD is in good agreement with values previously reported (12). This rate constant for Cu,Zn-SOD is per dimer, whereas that for dismutation by Cygb is per monomer, so for similar comparison, the rate constant for $O_2^{\bullet-}$ dismutation by each Cu,Zn-SOD monomer would be 6.0×10^8 $M^{-1} \cdot s^{-1}$.

In order to determine how the SOD activity of Cygb compared to that of other globins, additional comparative measurements were performed for the other three mammalian globins: Hb, Mb, and neuroglobin (Ngb). With 1 μM globin concentration, while Cygb quenches the initial rate of $O_2^{\bullet-}$ generation by over 90%, Hb, Mb, or Ngb had no significant effect, indicating >100-fold lower SOD activity than Cygb (*SI Appendix*, Fig. S1).

Electron Paramagnetic Resonance Spin-Trapping Measurements of SOD Function. While the cyt *c* reduction assay is well established for the measurement of $O_2^{\bullet-}$, it has limited specificity. There could be inaccuracies due to modest levels of direct electron transfer from reduced Cygb or XO to cyt *c*. In order to provide a more direct and definitive assay of the rate of Cygb-mediated SOD function and efficacy relative to known SOD enzymes, electron paramagnetic resonance (EPR) spin-trapping experiments were performed with the $O_2^{\bullet-}$ generating system, XO and X. XO (0.1 μM) and X (300 μM) were mixed in phosphate-buffered saline (PBS) and 0.1 mM ethylenediaminetetraacetic acid (EDTA), pH 7.4, buffer at room temperature (RT) in the absence (V_0) or presence (V_i) of varying concentrations of Cygb from 1 nM to 50 nM. $O_2^{\bullet-}$ production was measured from the formation of the trapped $O_2^{\bullet-}$ adduct, DIPPMPO-OOH. The amount and rate of $O_2^{\bullet-}$ generation was determined from the time-dependent increase in $O_2^{\bullet-}$ adduct signal

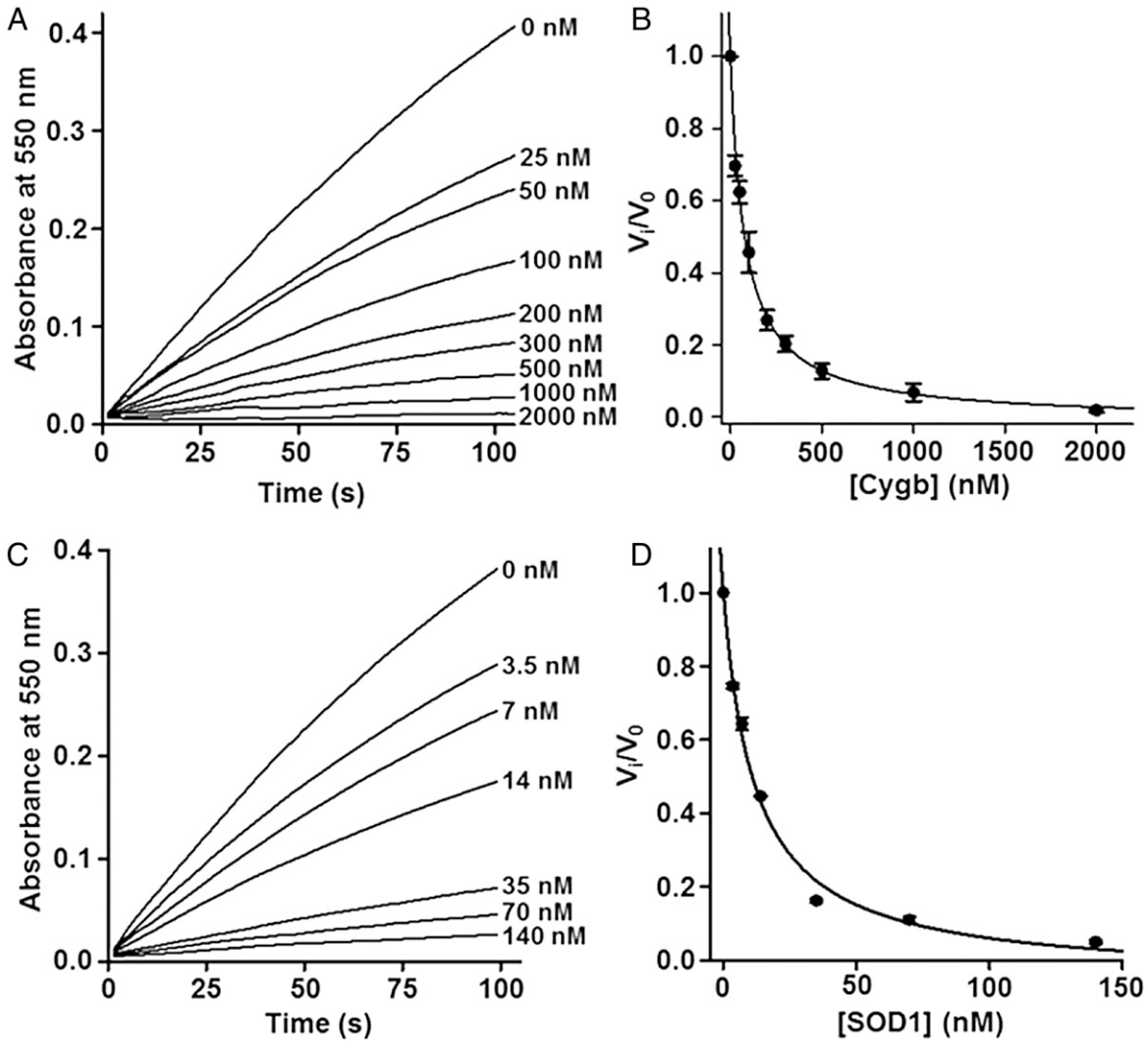

Fig. 2. Measurement of the SOD activity of Cygb and Cu,Zn-SOD assayed by ferricytochrome *c* reduction. The reaction mixture contained 50 μM ferricytochrome *c*, 50 μM X, and 0.1 mM EDTA in 50 mM phosphate buffer (pH 7.8) and was initiated by adding XO (70 nM final concentration). Increase in optical absorbance at 550 nm was followed in the absence or presence of various concentrations of Cygb (*A*) or Cu,Zn-SOD (SOD1) (*C*) with initial rates of cyt *c* reduction measured in the absence (V_0) and presence (V_i) of Cygb or Cu,Zn-SOD. Graphs of the concentration-dependent inhibition of the rate of cyt *c* reduction by Cygb (*B*) or Cu,Zn-SOD (*D*). Graphs show the mean ± SEM of three independent measurements fitted with nonlinear regression.

over the first 7 min after initiation of the reaction with addition of X to XO using 10 mM DIPPMPO (Fig. 3 *A* and *B*). Cygb dose dependently quenched the $O_2^{\bullet-}$ adduct signal with 50% decrease seen at 2.80 ± 0.42 nM Cygb, determined from a hyperbolic fit to the ratio of the rates (V_i/V_0) for DIPPMPO-OOH formation. Thus, Cygb clearly functions as an enzyme that cycles to catalytically degrade $O_2^{\bullet-}$. The rate constant of $O_2^{\bullet-}$ trapping by DIPPMPO is estimated to be ~45 $M^{-1} \cdot s^{-1}$ at pH 7.4, similar to DEPMPO, which has a value 1.5-fold that of 5,5-dimethyl-1-pyrroline-N-oxide (DMPO) (13, 14). Therefore, we estimate the rate of $O_2^{\bullet-}$ dismutation to be (1.61 ± 0.24) × 10^8 $M^{-1} \cdot s^{-1}$ based on the product of the ratio of the DIPPMPO concentration to the concentration of protein exhibiting 50% inhibition and the bimolecular rate constant for the reaction between $O_2^{\bullet-}$ and DIPPMPO.

Similar spin-trapping measurements were performed with Cu,Zn-SOD and Mn-SOD to compare their rates of $O_2^{\bullet-}$ dismutation to that of Cygb. As seen in Fig. 3 *C* and *E*, Cu,Zn-SOD (labeled SOD1) and Mn-SOD (labeled SOD2) similarly quenched the characteristic DIPPMPO-OOH adduct in a dose-dependent manner. For Cu,Zn-SOD (Fig. 3 *C* and *D*), a 50% decrease in signal occurred at 0.28 ± 0.04 nM. This is 10-fold lower than the Cygb concentration that provided comparable quenching, giving a rate of $O_2^{\bullet-}$ dismutation of (1.60 ± 0.23) × 10^9 $M^{-1} \cdot s^{-1}$. This value is consistent with the rates for enzymatic dismutation of $O_2^{\bullet-}$ in the literature (12, 15). This rate also compares favorably with that determined from the cyt *c* assay for SOD function. For Mn-SOD, a 50% decrease in signal was seen at 0.79 ± 0.01 nM (Fig. 3 *E* and *F*), ~2.8-fold higher than Cu,Zn-SOD. This indicates a rate constant for $O_2^{\bullet-}$ dismutation by Mn-SOD of (5.70 ± 0.05) × 10^8 $M^{-1} \cdot s^{-1}$, only ~3.3-fold higher than that by Cygb. Cu,Zn-SOD and Mn-SOD are both dimers. For comparison with Cygb, the second-order rate constants for Cu,Zn-SOD and Mn-SOD per monomer are 8.0 × 10^8 $M^{-1} \cdot s^{-1}$ and 2.85 × 10^8 $M^{-1} \cdot s^{-1}$, respectively, and only approximately fivefold and twofold greater than the rate of dismutation by Cygb.

Stopped-Flow Measurements of the Rate of $O_2^{\bullet-}$ Dismutation. Stopped-flow experiments were performed to determine the bimolecular rate constants for $O_2^{\bullet-}$ dismutation by Cygb, Cu,Zn-SOD, and Mn-SOD from the slope of the linear plot of k_{obs}

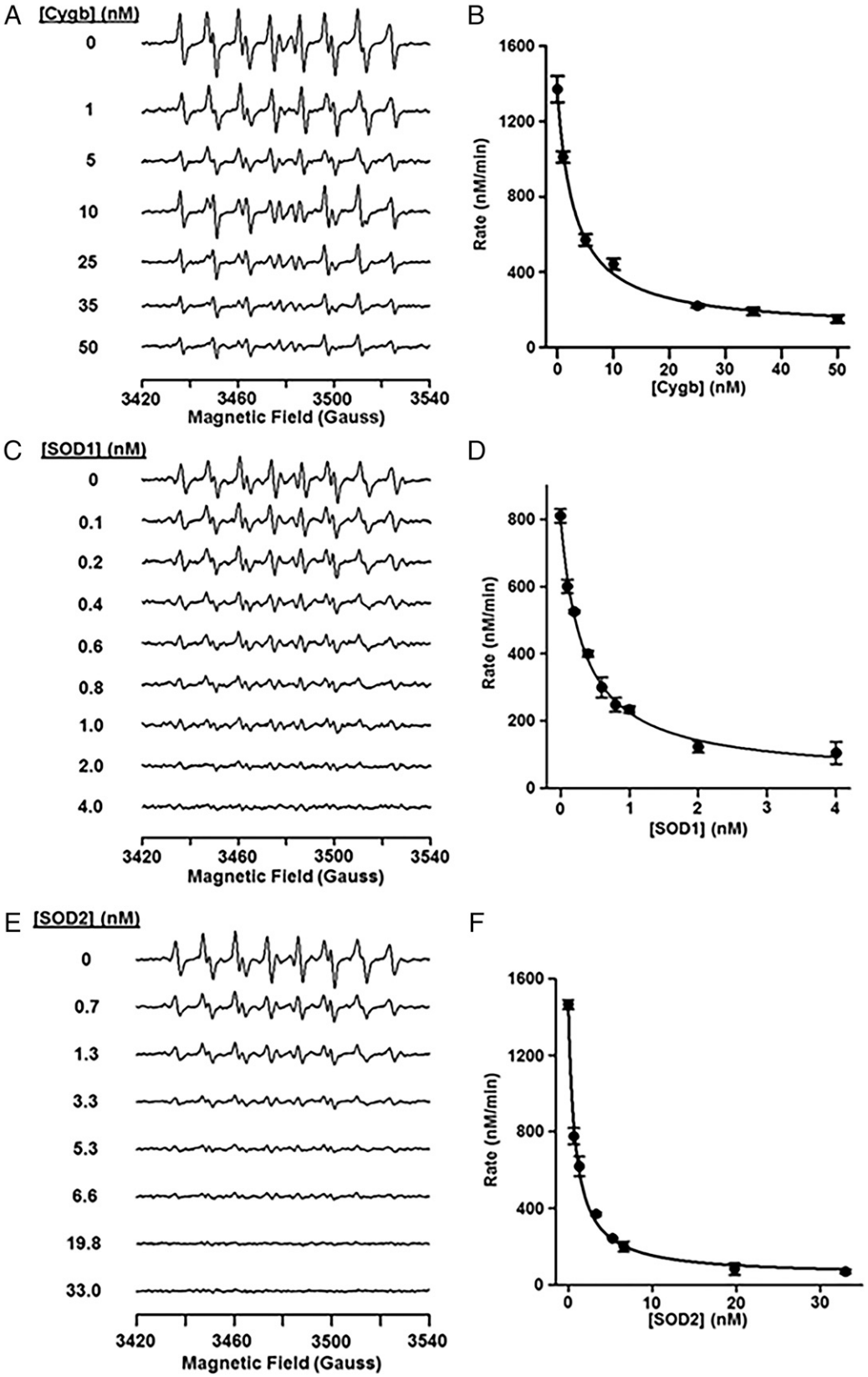

Fig. 3. EPR measurements of the decrease in the rate of $O_2^{\bullet-}$ trapping with increasing concentrations of Cygb, Cu,Zn-SOD, or Mn-SOD. Stack plots of the EPR signal observed as a function of protein concentration are shown for Cygb (*A*), Cu,Zn-SOD (SOD1) (*C*), and Mn-SOD (SOD2) (*E*) ~5 min after initiating the X/XO reaction. Initial rates of formation of the DIPPMPO-OOH signal were determined in the absence (V_0) and presence (V_i) of various concentrations of Cygb (*B*), Cu,Zn-SOD (*D*), and Mn-SOD (*F*). Each data point is the mean ± SEM of three measurements and fitted with a hyperbolic function.

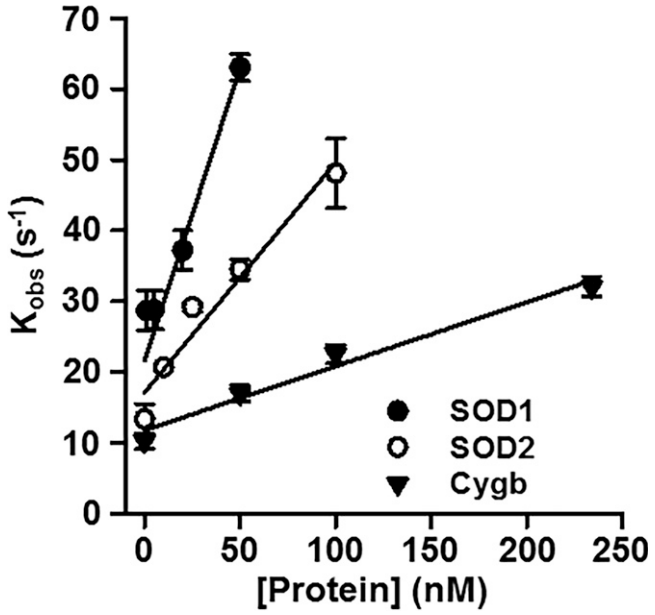

Fig. 4. Rates of $O_2^{\bullet-}$ decay measured by stopped-flow spectroscopy for Cu,Zn-SOD, Mn-SOD, and Cygb. The $O_2^{\bullet-}$ absorbance was monitored at 245 nm for Cu,Zn-SOD (SOD1), Mn-SOD (SOD2), and Cygb in 100 mM Hepes and 0.1 mM EDTA, pH 7.8, at RT. The slope of the plot of k_{obs} versus [protein] yielded the bimolecular dismutation rate for each protein: Cu,Zn-SOD ~1.0×10^9 $M^{-1} \cdot s^{-1}$, Mn-SOD ~5.3×10^8 $M^{-1} \cdot s^{-1}$, and Cygb ~1.0×10^8 $M^{-1} \cdot s^{-1}$. The data shown are the mean ± SEM of at least five independent measurements.

versus [protein] (Fig. 4). From the slopes of the plots in Fig. 4, the bimolecular dismutation rate constants for Cygb, Cu,Zn-SOD, and Mn-SOD are ~1.0×10^8 $M^{-1} \cdot s^{-1}$, 1.0×10^9 $M^{-1} \cdot s^{-1}$, and 5.3×10^8 $M^{-1} \cdot s^{-1}$, in very good agreement with the EPR and cyt *c* assay results, with the monomeric Cu,Zn-SOD rate of $O_2^{\bullet-}$ dismutation approximately fivefold greater than Cygb and the monomeric Mn-SOD rate ~2.6-fold greater.

Cygb-Mediated $O_2^{\bullet-}$ Dismutation Is Inhibited by CN or CO Binding. EPR spin-trapping experiments were performed to assess whether complexation of the ferric and ferrous states of Cygb inhibited its SOD function. X/XO was used to generate $O_2^{\bullet-}$ as in Fig. 3. With no Cygb present, a prominent DIPPMPO-OOH signal was seen that was totally quenched by 50 nM Cygb (Fig. 5*A*). With CN complexation of Fe^{3+}-Cygb, ~90% restoration of the signal occurred, and with CO complexation of Fe^{2+}-Cygb, there was ~70% restoration (Fig. 5*B*). Thus, both ferric and ferrous heme complexation inhibit the SOD function of Cygb.

Optical Absorption Measurements of the Reactions of $O_2^{\bullet-}$ with Ferric and Ferrous Cygb. $CygbFe^{3+}$ exhibits a Soret band peak at 416 nm and α/β region peaks at 533 and 563 nm (Fig. 6*A*). Upon anaerobic reduction of the heme iron with stoichiometric 1:1 addition of dithionite, the Soret band shifts to 428 nm and the α/β region peaks shift to 532 and 560 nm, indicative of the formation of Fe^{2+}-Cygb. With exposure of Fe^{2+}-Cygb to oxygenated buffer, O_2 binds and the Soret peak shifts to 417 nm with α/β region peaks at 540 and 578 nm, indicative of the formation of $CygbFe^{2+}$-O_2. Thus, each redox state of Cygb exhibits distinguishable optical absorption spectra.

Experiments were performed to characterize the reaction of $CygbFe^{2+}$-O_2 with $O_2^{\bullet-}$, and with stoichiometric ~1:1 addition of potassium superoxide (KO_2) and measurement of the absorption spectra every 0.5 s, the spectrum immediately shifted to that of $CygbFe^{3+}$ with Soret peak at 416 nm and α/β region peaks at 533 and 563 nm (Fig. 6*B*). With repeat spectral acquisitions and repeated additions of KO_2, no further spectral changes were seen with curves superimposed on the initial spectrum.

Experiments were then performed to characterize the reaction of $CygbFe^{3+}$ with $O_2^{\bullet-}$. With stoichiometric ~1:1 addition of KO_2 and measurement of the absorption spectra every 0.5 s, only very small trace spectral changes were seen without further change with repeat spectral acquisitions or repeated additions of KO_2 (Fig. 6*C*). The failure to see major spectral shifts to the spectrum of $CygbFe^{2+}$-O_2, indicating a lack of accumulation of this state, may be due to a much faster reaction of $O_2^{\bullet-}$ with $CygbFe^{2+}$-O_2 compared to that with $CygbFe^{3+}$. In consideration of this, in an effort to detect whether $O_2^{\bullet-}$ reacts to reduce $CygbFe^{3+}$, experiments were performed with addition of $O_2^{\bullet-}$ to $CygbFe^{3+}$ in the presence of a large excess of CO. Under anaerobic conditions with stoichiometric ~1:1 addition of KO_2 to $CygbFe^{3+}$ in CO-saturated buffer and measurement of the absorption spectrum, a clear shift in the heme Soret region from 416 nm to 420 nm along with shifts in the α/β region from 533 to 541 nm and 563 to 569 nm with increased absorption was seen, indicative

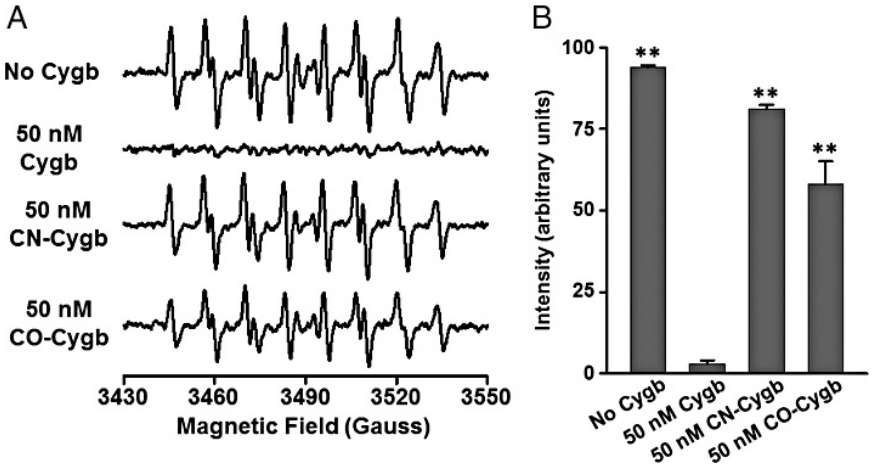

Fig. 5. Binding of CN or CO to the Fe^{3+} or Fe^{2+} heme inhibits Cygb-mediated $O_2^{\bullet-}$ dismutation. EPR spin-trapping was performed using DIPPMPO in the presence of X and XO as described in Fig. 3. (*A*) Spectra shown are 40-s acquisitions acquired after ~2 min of the reaction. (*B*) Relative intensities from the EPR spectra in *A*. While 50 nM Cygb quenches the observed $O_2^{\bullet-}$ radical adduct generation, this is largely abolished with CN-Fe^{3+}-Cygb (CN-Cygb) or CO-Fe^{2+}-Cygb (CO-Cygb). Thus, either complexation of CN to the ferric heme or CO to the ferrous heme blocks the SOD activity of Cygb. Data are the mean ± SEM, $n = 10$ to 14. $^{**}P < 0.01$ versus 50 nM Cygb.

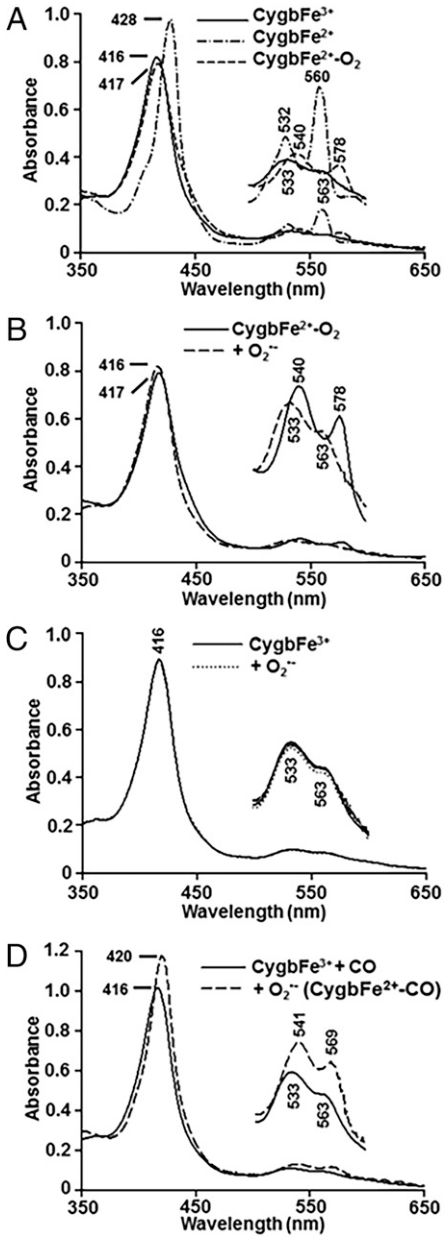

Fig. 6. Spectrophotometric measurements of the reaction of Cygb with $O_2^{\bullet-}$. (*A*) The spectrum of $CygbFe^{3+}$ (10 μM) with Soret peak at 416 nm and α/β peaks at 533 and 563 nm (solid line). After addition of dithionite, $CygbFe^{2+}$ is formed with shift of Soret peak to 428 nm and α/β peaks to 532 and 560 nm (dash dot line), and following subsequent introduction of O_2, $CygbFe^{2+}$-O_2 is formed with Soret peak at 417 nm and α/β peaks at 540 and 578 m (dashed line). (*B*) Stiochiometric addition (1:1) of KO_2 to $CygbFe^{2+}$-O_2 (solid line), formed as in *A*, triggers a shift back to $CygbFe^{3+}$ (dashed line). (*C*) Addition (1:1) of KO_2 to $CygbFe^{3+}$ (solid line) results in only trace change in the spectra (dotted line), and with further addition of KO_2, no further spectral changes were seen. From the minimal spectral change, it is estimated that less than 10% of $CygbFe^{3+}$ is converted to $CygbFe^{2+}$-O_2. (*D*) Upon repeat of the experiment in *C* in the presence of CO-saturated buffer, the Fe^{3+}Cygb spectrum is converted to that of $CygbFe^{2+}$-CO (dashed line), with a Soret band shift to 420 nm, and shifts in the α/β region to 569 nm/541 nm, respectively, with increased absorbance. With further addition of KO_2, no further spectral changes were seen. Thus, $O_2^{\bullet-}$ reduces Cygb from the ferric to the ferrous state, which is stabilized by CO binding. As shown in *C*, in the absence of CO, little $CygbFe^{2+}$-O_2 accumulates, likely due to further rapid reaction with $O_2^{\bullet-}$. Spectra of 0.5 s were recorded with mixing and start of spectral acquisition within ~4 s. For each experiment, the reactions were completed in the initial spectrum as depicted with no further changes in repeat scans.

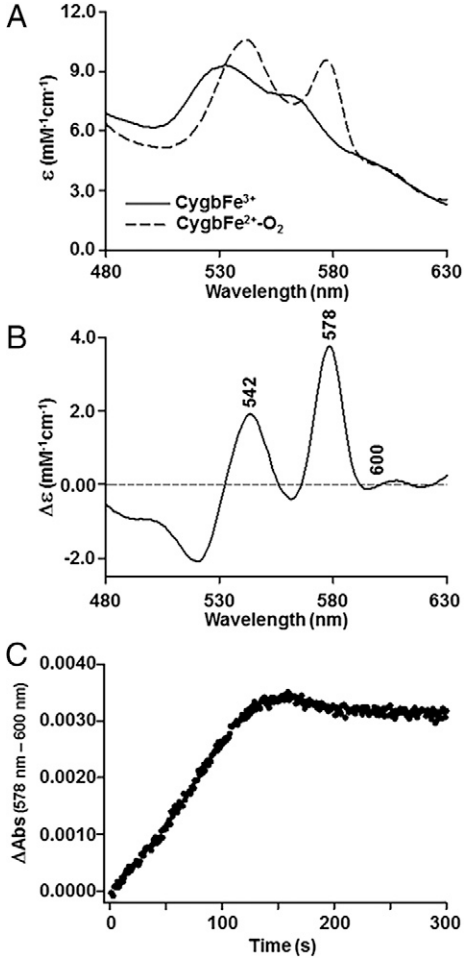

Fig. 7. Spectra of $CygbFe^{3+}$ and $CygbFe^{2+}$-O_2 and measurement of $CygbFe^{2+}$-O_2 formation with constant flux of $O_2^{\bullet-}$. Spectra (*A*) and difference spectra (*B*) of the α/β region of $CygbFe^{3+}$ and $CygbFe^{2+}$-O_2. (*C*) Measurement of $CygbFe^{2+}$-O_2 formation from $CygbFe^{3+}$ (24 μM) in the presence of constant $O_2^{\bullet-}$ generation from XO (1 μM) and X (400 μM). A maximum of ~4% of the Cygb was converted to $CygbFe^{2+}$-O_2.

of the formation of $CygbFe^{2+}$-CO (Fig. 6*D*). This spectral change occurred immediately following addition of KO_2 and remained unchanged with subsequent spectral acquisitions or following further addition of KO_2. Thus, $O_2^{\bullet-}$ reduces ferric Cygb to the ferrous state, which is stabilized by CO binding.

From the experiments in Fig. 6, the rate of the reaction of $O_2^{\bullet-}$ with $CygbFe^{2+}$-O_2 would be expected to be >10-fold faster than that with $CygbFe^{3+}$ so that $CygbFe^{2+}$-O_2 formed rapidly reacts with a second $O_2^{\bullet-}$ to return to the ferric state with only a low proportion of this species present. In order to confirm this and to estimate the ratio of the rate constants for step 1 and step 2 of the dismutation reaction scheme (Eq. **1**), we performed kinetics experiments reacting $CygbFe^{3+}$ (24 μM) with a steady flux of $O_2^{\bullet-}$ formed by XO (1 μM) and X (400 μM) in the presence of catalase (900 U/mL) with reaction performed in O_2 purged phosphate buffer. A constant flux of $O_2^{\bullet-}$ generation is produced for over 300 s with total formation of ~200 μM $O_2^{\bullet-}$, as assayed by cyt *c* reduction. X was added to start the reaction and optical absorption measurements performed every 0.5 s. As shown in Fig. 6*A* and expanded in Fig. 7*A*, while the Soret bands of $CygbFe^{3+}$ and $CygbFe^{2+}$-O_2 are similar, there are distinct differences in the α/β region. As seen in the difference spectrum (Fig. 7*B*), $CygbFe^{2+}$-O_2 exhibits higher absorption peaks at 542 and 578 nm with maximum difference at 578 nm, while 600 nm

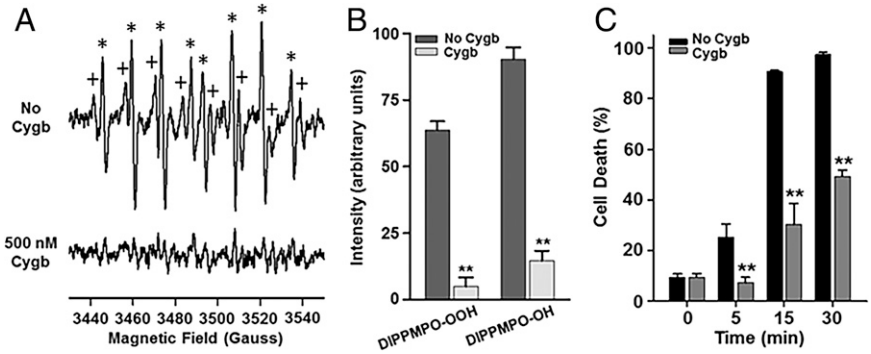

Fig. 8. Addition of Cygb quenches extracellular radical generation and prevents cell death. SMCs, 2×10^6/mL, were incubated with the $O_2^{\bullet-}$ generating system X, 300 μM, and XO, 0.1 μM, and (X/XO) with or without 0.5 μM Cygb. (*A*) EPR spin-trapping was performed in the presence of 10 mM DIPPMPO, with spectra shown recorded ~5 min postaddition of X/XO. Prominent signals of DIPPMPO-OOH peaks labeled (+) and DIPPMPO-OH peaks labeled (⋆) were seen that were quenched in the presence of Cygb. (*B*) Bar graph of the data from triplicate experiments as in *A*. (*C*) Data from parallel experiments measuring cell death by trypan blue exclusion with measurements at 5 and 15 min postaddition of X/XO. Increase in cell death was seen with exposure to the radical-generating system that was decreased by Cygb. Thus, Cygb addition quenched the radical generation and decreased radical-induced cell death. Data are the mean ± SEM, $n = 3$. $^{**}P < 0.01$ versus No Cygb.

is an isosbestic point. Therefore, to detect any transformation of $CygbFe^{3+}$ to $CygbFe^{2+}$-O_2, we monitored the absorption change at 578 nm relative to 600 nm (Fig. 7*B*). After addition of X, an absorbance increase of 0.0035 au was seen corresponding to 3.8% of the Cygb as $CygbFe^{2+}$-O_2 (Fig. 7*C*). In repeat experiments ($n = 4$), similar results were obtained with absorbance increases corresponding to 3.4 to 4.2% $CygbFe^{2+}$-O_2. As detailed in *Discussion*, from this experiment, the relative rate constants for each of the proposed steps in the dismutase reaction can be estimated.

Cygb Protects SMCs against $O_2^{\bullet-}$-Mediated Stress. In order to determine whether Cygb can protect cells against $O_2^{\bullet-}$-mediated oxidant stress, experiments were first performed exposing cultured, human aortic SMCs to an extracellular X/XO $O_2^{\bullet-}$-generating system in the presence or absence of 0.5 μM Cygb. Parallel measurements of $O_2^{\bullet-}$ and cell death were performed using spin-trapping in the presence of DIPPMPO (10 mM) or trypan blue exclusion, respectively. $O_2^{\bullet-}$ and $O_2^{\bullet-}$-derived radical generation was seen with DIPPMPO-OOH and DIPPMPO-OH adducts. In the presence of Cygb, radical adduct generation was largely

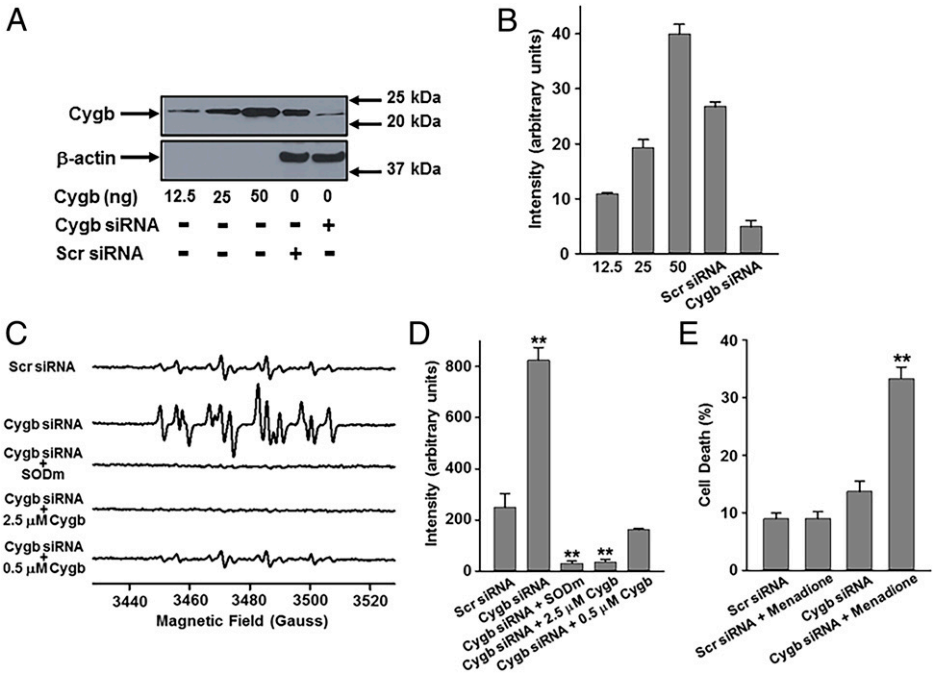

Fig. 9. Effect of Cygb expression on menadione-induced intracellular $O_2^{\bullet-}$ generation and cell death. Cygb expression was knocked down in SMCs using Cygb siRNA with matched Scr siRNA control. (*A* and *B*) With siRNA treatment, Cygb expression was decreased by ~85% compared to the Scr siRNA control SMCs. (*C*) EPR spin-trapping of menadione-treated SMCs showed that menadione induced $O_2^{\bullet-}$-mediated radical generation that was increased in the Cygb siRNA–treated SMCs in which Cygb expression was knocked down. (*D*) From triplicate experiments, Cygb KD increased the observed radical generation by over threefold. This radical generation was quenched by an SOD_m that enters cells, M40403 (50 μM). When these cells were preincubated with Cygb either 0.5 or 2.5 μM, radical generation was also decreased. (*E*) From parallel experiments measuring cell death by trypan blue uptake, with measurements at 30 min postmenadione addition, cell death increased in Cygb siRNA–treated cells but not in control Scr siRNA–treated cells. Thus, KD of Cygb increased the levels of $O_2^{\bullet-}$ detected, and this correlated with increased cell death. Data are the mean ± SEM, $n = 3$. $^{**}P < 0.01$ versus Scr siRNA.

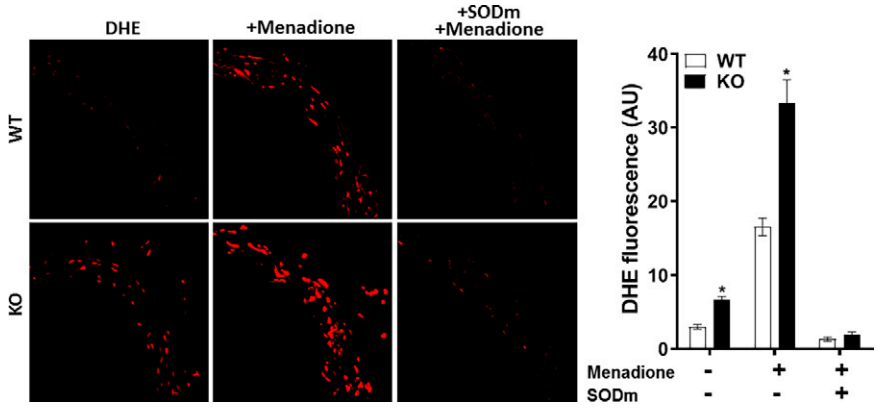

Fig. 10. Effect of Cygb-KO on menadione-induced $O_2^{\bullet-}$ generation in aorta of WT and *Cygb*$^{-/-}$ mice. Aortic sections from C57BL/6 (WT) and *Cygb*$^{-/-}$ (KO) mice were incubated with 10 μM DHE alone, 10 μM menadione plus DHE, or with 100 μM SOD_m (GC4419) together with DHE and menadione. Sections were visualized with confocal fluorescence microscopy. As seen in the images, red fluorescence arises from $O_2^{\bullet-}$-mediated oxidation of DHE. The bar graph shows quantitation of the fluorescence from a series of repeat measurements. Incubation with SOD_m quenched the observed fluorescence, confirming that it is $O_2^{\bullet-}$ derived. The menadione-induced $O_2^{\bullet-}$ generation in aortic sections was much higher in Cygb-KO aorta compared to WT. Data shown are the mean ± SEM, $n = 6$. *$P < 0.01$ versus WT.

quenched with over 80% decrease (Fig. 8 *A* and *B*). In parallel with this, the time-dependent increase in cell death in the presence of the $O_2^{\bullet-}$-generating system was decreased by over 60%, from ∼91% down to ∼30% after 15 min (Fig. 8*C*). Thus, Cygb was highly effective in quenching extracellular $O_2^{\bullet-}$ radical generation and preventing related cell death.

Since Cygb is normally present within the cell cytosol, we performed further experiments to determine the function of intrinsically expressed Cygb in SMCs and, with small interfering RNA (siRNA)–mediated knockdown (KD), its role in quenching stimulated intracellular $O_2^{\bullet-}$ generation and preventing cell death. In order to determine the levels of Cygb expressed in these cells, quantitative immunoblotting was performed using known concentrations of purified Cygb and cell homogenate. From these studies, we estimated that 68 ng of Cygb was present in 80 μg SMC homogenate corresponding to an intracellular concentration of ∼4.9 μM (Fig. 9 *A* and *B*). This level is consistent with values of 3 to 5 μM previously measured in rat SMCs (16). siRNA-mediated KD decreased Cygb expression by ∼85%, while control scrambled siRNA (Scr siRNA) had little effect (left columns in Fig. 9 *A* and *B*). With similar quantitative Western blotting for Cu,Zn-SOD, its expression was approximately eightfold lower than Cygb, and Mn-SOD was ∼48-fold lower. (*SI Appendix*, Fig. S2). Thus, Cygb would be expected to impact intracellular $O_2^{\bullet-}$ catabolism in normal SMCs.

In order to stimulate intracellular $O_2^{\bullet-}$ production, SMCs were treated with the uncoupler menadione (50 μM), and spin-trapping studies were performed with DMPO. As seen in control Cygb-containing cells treated with Scr siRNA, menadione treatment stimulated radical generation (upper line, Fig. 9*C* and left bars, Fig. 9*D*). With Cygb KD cells, this radical generation increased over threefold, and a prominent DMPO-OOH signal of the $O_2^{\bullet-}$ adduct was seen (second line, Fig. 9*C*). With preaddition of the SOD mimetic (SOD_m) M40403 (50 μM) (17) to menadione-treated Cygb KD cells, the observed radical generation was totally quenched. Similarly, when the SMCs were preincubated for 60 min with 2.5 μM Cygb, the radical generation was greatly decreased. With preincubation with 0.5 μM Cygb, a lesser, approximately fourfold decrease in radical generation was present (Fig. 9 *C* and *D*). Thus, the levels of Cygb in untreated or Scr siRNA–treated SMCs function to quench intracellular $O_2^{\bullet-}$ generation, and when Cygb is depleted, $O_2^{\bullet-}$ increases markedly.

In order to determine whether intrinsic Cygb levels also protect against intracellularly generated $O_2^{\bullet-}$-mediated cell death, experiments were performed measuring trypan blue exclusion after 30 min of menadione exposure. In Scr siRNA–treated cells, 9.0 ± 1.0% cell death was seen with no increased postmenadione treatment. In contrast, 13.7 ± 1.8% cell death was seen in basal Cygb siRNA cells with an increase to 33.3 ± 2.0% cell death post-treatment (Fig. 9*E*). Thus, intrinsic Cygb expression in SMCs protects these cells against basal and stimulated $O_2^{\bullet-}$ generation.

Since Cygb is highly expressed in the SMCs of the vascular wall and has an important role in regulating vascular tone (16, 18), experiments were performed measuring $O_2^{\bullet-}$-production in aortic sections from *Cygb*$^{-/-}$ (KO) and wild-type (WT) mice using the fluorescent dye dihydroethidium (DHE) that reacts with $O_2^{\bullet-}$, giving rise to characteristic red fluorescence (19–21). Low levels of DHE-derived fluorescence were seen in *Cygb*$^{-/-}$ vessels but not in WT (Fig. 10) (refer also to *SI Appendix*, Fig. S3 with superimposed DAPI nuclear stain). With addition of menadione (10 μM), fluorescence increased over fourfold in the *Cygb*$^{-/-}$ vessels (KO), while levels in the WT increased but were more than twofold lower than those with Cygb gene knockout (Cygb-KO). Addition of the SOD_m quenched the observed fluorescence, confirming that it was derived from $O_2^{\bullet-}$. Thus, Cygb in the SMCs of the vascular wall exerts SOD function, which is lost with genetic knockout, and this SOD function provides protection against both basal and stimulated $O_2^{\bullet-}$ generation.

Discussion

Cygb is a six-coordinate globin with multiple important properties and proposed roles in cellular physiology and homeostasis (1, 4–6). It was first identified in the stellate cells of the liver and also shown to be expressed in fibroblast and SMC lines (2). When reduced, it rapidly degrades NO in a highly O_2-dependent manner that could contribute to O_2 sensing and hypoxic vasodilation (16, 22). It also serves as a nitrite reductase forming NO under anoxic conditions (23). Increasing data have emerged demonstrating that Cygb may play a prominent role in antioxidative defense; however, the basis for this has not been well understood (8).

Rh-Cygb has been shown to exert protective antioxidative effects on chronic alcohol-induced liver disease (ALD) by suppressing lipopolysaccharide (LPS)–induced Kupffer cell proliferation and TNF-α expression (24). A decrease in LPS-induced NO and $O_2^{\bullet-}$ production was also observed with rh-Cygb treatment (24). Cygb was also shown to prevent atherosclerosis by regulating lipid metabolism and protecting cells from injury caused by oxidative stress (25). Based on this, Cygb has been proposed to be a promising therapeutic candidate for prevention of ALD

and atherosclerosis (24, 25). A tumor suppressor role of Cygb through ROS regulation has also been postulated (26).

Despite the strong evidence for a role of Cygb in antioxidative protection and the central role of $O_2^{\bullet-}$ in oxidative stress, there has been controversy regarding the SOD function of Cygb. There have been two conflicting prior reports in this regard. The first study claimed to show a lack of activity based on assays at pH 9 using lucigenin luminescence (27); however, measurements were only performed at this strong alkaline pH with the use of lucigenin that is now known to uncouple a variety of flavo-enzymes including endothelial nitric oxide synthase (eNOS) and XO with stimulation of $O_2^{\bullet-}$ generation (28, 29). The second study (30) used the fluorescence probe 4, 5-dimethoxy-2-nitro-benzenesulfonyl tetrafluorofluorescein (BESSo) (31) and concluded that Cygb has high $O_2^{\bullet-}$-scavenging ability, but they inferred this to be well below that of Cu,Zn-SOD, even though no comparative studies of Cygb and Cu,Zn-SOD were performed. The fluorescence technique used is at best qualitative for $O_2^{\bullet-}$ detection and is affected by ferrous iron and flavin centers (31). Thus, while it is clear that Cygb exerts antioxidative protection, controversy has remained regarding its SOD function.

From the current studies, we observe that Cygb is an efficient SOD with a high bimolecular dismutation rate constant on the order of 10^8 $M^{-1} \cdot s^{-1}$, only about fivefold less than that of Cu,Zn-SOD on a monomer basis and comparable to that for Mn-SOD and a range of bacterial SODs. Literature values of the rate constant for Cu,Zn-SOD are in the range of (5 to 10) $\times$ 10^8 $M^{-1} \cdot s^{-1}$ (15, 32) and (3 to 9) $\times$ 10^8 $M^{-1} \cdot s^{-1}$ for Mn-SOD from *E. coli* (33, 34). As such, Cygb could be considered as a novel class of $O_2^{\bullet-}$ dismutating protein in mammalian cells and protein in the globin family with this functionality. We observed that the SOD function of Cygb was inhibited by cyanide, which coordinates to $CygbFe^{3+}$, and by CO, which coordinates to $CygbFe^{2+}$. Spectrophotometric measurements demonstrated that $O_2^{\bullet-}$ reacts with $CygbFe^{3+}$ with formation of $CygbFe^{2+}$, which in the presence of CO is trapped as $CygbFe^{2+}$-CO (Fig. 6*D*). With similar measurements in the absence of CO, only a small fraction of $CygbFe^{2+}$-O_2 was present. Furthermore, $O_2^{\bullet-}$ was shown to react with $CygbFe^{2+}$-O_2 to regenerate Fe^{3+}-Cygb completing the process of superoxide dismutation (Fig. 6*B*). Thus, our results suggest the following reaction scheme (Eq. 1):

$$CygbFe^{3+} + O_2^{\bullet-} \xrightarrow{k_1} \left[CygbFe^{3+}\text{—}O_2^{\bullet-} \rightleftharpoons CygbFe^{2+}\text{—}O_2\right] \xrightarrow[O_2^{\bullet-}\ 2H^+]{k_2} CygbFe^{3+} + H_2O_2 + O_2$$

$$\text{net reaction:}\quad CygbFe^{3+} + 2O_2^{\bullet-} \xrightarrow{2H^+} CygbFe^{3+} + H_2O_2 + O_2 \qquad [1]$$

This reaction scheme is somewhat similar to that previously described for $O_2^{\bullet-}$ dismutation by Hb (35); however, for Cygb, this process is much faster as seen in our comparative studies of the rates of $O_2^{\bullet-}$ dismutation by different globins (*SI Appendix*, Fig. S1). In view of the low amount of $CygbFe^{2+}$-O_2 present following bolus addition or sustained generation of $O_2^{\bullet-}$, the rate of the second step, k_2, would be predicted to be much faster than the first step, k_1. Under steady-state (ss) conditions with sustained $O_2^{\bullet-}$ generation, only ~4% $CygbFe^{2+}$-O_2 was detected, which in turn suggests that k_2 is 25-fold higher than k_1. Assuming ss conditions, utilizing the observed overall rate of $O_2^{\bullet-}$ dismutation (K_{obs}) of 1.6 $\times$ 10^8 $M^{-1} \cdot s^{-1}$, the individual rate constants for each step can be estimated from the measured levels of $CygbFe^{3+}$ and $CygbFe^{2+}$-O_2 (*SI Appendix*):

$$k_1 = k_{obs}[\text{Cygb}]/2 \times \left[\text{CytbFe}^{3+}\right]_{ss} = 0.83 \times 10^8 \text{M}^{-1}\text{s}^{-1}$$

$$k_2 = k_{obs}[\text{Cygb}]/2 \times \left[\text{CytbFe}^{2+}\text{O}_2\right]_{ss} = 2.1 \times 10^9 \text{M}^{-1}\text{s}^{-1}.$$

At this point, it is unclear why Cygb uniquely has this high rate of $O_2^{\bullet-}$ dismutation. Interestingly, crystal-structure modeling data suggested participation of Arg84 in ligand binding and its interaction with the iron-bound ligand of Cygb with rotation around the C^{α}–C^{β} bond of Arg-84, allowing movement of the guanidium group to within 3 Å of the iron atom and the sixth coordination site (36). Furthermore, based on infrared and Raman spectroscopic data, interaction of the positively charged guanidinium group of Arg84 with iron-bound CO was proposed (37). These data have implied the involvement of Arg84 in the O_2- and CO-binding reactions. As such, Arg84 may be involved in $O_2^{\bullet-}$ binding and stabilization at the heme iron to facilitate the process of dismutation.

This identified novel SOD function of Cygb may be particularly important for protection against oxidative stress in cells containing high expression of the protein, such as liver stellate cells, pericytes of all organs, fibroblasts, or SMCs, in which Cygb concentrations have been reported to be as high as 5 μM. Furthermore, with hypoxia, Cygb expression has been shown to increase by over twofold (23, 38). In the present study, we observed that in isolated SMCs, the intrinsic levels of Cygb expression largely quenched the $O_2^{\bullet-}$ produced by addition of the uncoupler mendione. However, with siRNA-mediated KD of Cygb expression, of ~85%, an approximately threefold increase in the levels of $O_2^{\bullet-}$ detected by EPR spin-trapping was seen accompanied by ~2.4-fold increase in cell death (Fig. 9). Furthermore, studies measuring $O_2^{\bullet-}$ in the aorta of WT and $Cygb^{-/-}$ mice following menadione treatment, showed greater than twofold higher $O_2^{\bullet-}$-derived fluorescence in the vascular wall of $Cygb^{-/-}$ compared to WT (Fig. 10). Thus, the intrinsic levels of Cygb protect SMCs and vascular smooth muscle against stimulated $O_2^{\bullet-}$ generation and secondary injury.

In view of the presence of Cu,Zn-SOD and Mn-SOD in most cells, one would question why Cygb also has SOD function. Cygb also acts as a potent NO dioxygenase, serving as an important pathway for NO metabolism in the smooth muscle of the vascular wall, providing oxygen-dependent regulation of vascular tone (16, 22). The dual functions of catabolism of both NO and $O_2^{\bullet-}$ could serve as a key protective mechanism to prevent the formation of the potent oxidant, peroxynitrite ($ONOO^-$), which can be a key mediator of oxidative injury and protein nitration. Supporting this concept was the demonstration that nitrite and nitrate are elevated in the serum and urine of $Cygb^{-/-}$ mice relative to WT mice, with a concomitant increase in nitrotyrosine protein adducts, implying increased levels of $ONOO^-$ in these animals (39). This increased oxidative stress throughout the body of $Cygb^{-/-}$ mice resulted in multiple organ abnormalities (39).

An additional consideration is that Cygb in the ferrous-oxy state autoxidizes with a half-life of only several minutes (40). Its SOD function would efficiently convert $O_2^{\bullet-}$ to hydrogen peroxide that could exert a signaling role or be degraded by cellular peroxidases such as catalase, glutathione peroxidase, or others. Furthermore, since there are mechanisms that can serve to inactivate the activity of Cu,Zn-SOD and Mn-SOD, particularly under conditions of major oxidant stress, an additional backup mechanism of $O_2^{\bullet-}$ dismutation may be needed and would serve to protect the cell. Cu,Zn-SOD can be inactivated by hydrogen peroxide at high levels due to

oxidation of its catalytic histidine (41). Mn-SOD has been shown to have down-regulated activity due to acetylation and also can be inactivated by oxidative or nitrative stress (42–44). In contrast, Cygb is resistant to hydrogen peroxide, with peroxidase function due to hexacoordination of the heme iron atom (2, 45), and should also be highly efficient in preventing $ONOO^-$ formation, providing additional antioxidative protection.

In summary, we have identified a novel function of Cygb as an efficient SOD with a high bimolecular dismutation rate on the order of 10^8 $M^{-1} \cdot s^{-1}$. Cygb is unique as an Fe-centered SOD in mammalian cells and could be considered as a fourth type of SOD protein. It is also the only member of the globin family shown to have potent SOD activity. This SOD function of Cygb may serve to explain the prior reports of its antioxidative activity and the toxicities and disease seen with its genetic deletion, including the increased incidence of tumors. Combined with its potent NO dioxygenase activity, Cygb would be highly effective in decreasing both $O_2^{\bullet-}$ and NO levels, serving to decrease the formation of $ONOO^-$ and secondary oxidative injury. Future studies will be needed to further understand the role of this SOD function, its relationships to the other important functions of Cygb, and how this activity serves to regulate cellular physiology and disease.

Materials and Methods

Materials. The spin trap, DIPPMPO, was purchased from Alexis (Carlsbad), DMPO from Dojindo (Gaithersburg), and KO_2 from Alfa Aesar. XO from bovine milk, SOD from bovine liver (Cu,Zn-SOD), SOD from *E. coli* (Mn-SOD), and cyt *c* from equine heart were from MilliporeSigma. All other chemicals and reagents were of the highest quality commercially available and were from MilliporeSigma unless noted otherwise.

Expression and Purification of rh-Cygb. The expression plasmid for Cygb (human Cygb complementary DNA in pET3a) was obtained from Thorsten Burmester, University of Hamburg, Mainz, Germany, and transformed into *E. coli* strain C41(DE3)pLysS. Cells were grown overnight, and rh-Cygb was purified as described (16) (for details, refer to *SI Appendix, Methods*).

SDS PAGE. Purity of Cygb preparations were assayed at 4 °C on a reducing, graded (4 to 20%) Tris-glycine polyacrylamide gel (Invitrogen) at 125 V with Coomassie Blue staining as described (16). Protein band densities were quantified by a Pharos FX Plus Molecular Imager (Bio-Rad).

Western Blots. Whole-cell lysate or pure proteins were quantitated using the Bio-Rad detergent-compatible protein assay kit. Proteins were separated by SDS PAGE as above (*SDS PAGE*). Protein bands were transferred electrophoretically to a polyvinylidene fluoride (PVDF) membrane in 12 mM Tris·HCl, 96 mM glycine, and 20% methanol using a TE70X Semidry Transfer Unit (Hoefer) at 200 V for 2 h. The primary antibodies used were rabbit polyclonal anti-Cygb and mouse monoclonal β-actin, with anti-rabbit or anti-mouse horseradish peroxidase (HRP)–linked secondary antibodies (Santa Cruz Biotechnology). The membrane was blocked for 1 h at RT in Tris-buffered saline containing 0.05% Tween 20 (TBST) with 5% dried milk and incubated overnight with primary antibodies at 4 °C. The membrane was washed three times in TBST, incubated for 1 h with HRP-conjugated secondary in TBST at RT, and again washed three times in TBST. Protein bands were detected with enhanced chemiluminescence Western Blotting detection reagents (Amersham Biosciences) and exposed to X-ray film. Protein band densities were quantified by comparison to band densities of pure protein standards.

Protein Digestion for MS/Proteomics. Samples were resuspended in 50 mM ammonium bicarbonate with 5 μg/μL dithiothreitol and incubated at 56 °C for 15 min. Then iodoacetamide (15 mg/mL) was added and the sample kept in the dark at RT for 30 min. Sequencing-grade modified trypsin (Promega) was then added with ∼1:50 enzyme:substrate ratio and the reaction carried out at 37 °C overnight. Acetic acid was added to quench the reaction, and samples were dried in a vacuum centrifuge and resuspended in 20 μL of 50 mM acetic acid. Peptide concentration was determined by Nanodrop (A_{280nm}).

Capillary Liquid Chromatography–Nanospray Tandem MS. Capillary liquid chromatography–nanospray tandem MS of protein identification was performed on a Thermo Fisher Scientific Orbitrap Fusion mass spectrometer equipped with an EASY-Spray Source operated in positive ion mode as detailed in *SI Appendix, Methods*.

MALDI TOF MS. This was performed on an UltrafleXtreme MALDI TOF/TOF MS (Bruker Daltonics, Billerica) mass spectrometer operated in linear, positive ion mode at an accelerating voltage of 25 kV. The N_2 laser was operated at the minimum-threshold level required to generate signal and minimize dissociation. The instrument was calibrated with protein standards. The matrix, sinapinic acid, was prepared as a saturated solution in 50% acetonitrile with 0.1% trifluoroacetic acid in water. Aliquots of 5 μL of matrix and 1 μL of sample (20 μM) were thoroughly mixed, spotted on the target plate (1.0 μL), and allowed to dry before analysis. Scanning range was set at 10 to 50 kDa to allow detection of any protein dimers.

Measurements of SOD Activity. Commercial cyt *c* and XO were purified by passage through Sephadex G-25 pre-equilibrated with 50 mM phosphate buffer (pH 7.8) containing 0.1 mM EDTA. The XO concentration was determined from its absorbance at 450 nm using $\varepsilon_{450nm} = 37.8$ $mM^{-1} \cdot cm^{-1}$ (46) and its activity by monitoring the formation of uric acid at 295 nm using $\varepsilon_{295nm} = 9.6$ $mM^{-1} \cdot cm^{-1}$. The cyt *c* concentration was determined from its absorbance at 410 nm using $\varepsilon_{410} = 106$ $mM^{-1} \cdot cm^{-1}$ (47). X was freshly dissolved in 0.02 M potassium hydroxide and immediately used. The concentrations of Cu,Zn-SOD and Mn-SOD were determined from their corresponding extinction coefficients $\varepsilon_{258nm} = 10.3$ $mM^{-1} \cdot cm^{-1}$ (11) and $\varepsilon_{280nm} = 86.6$ $mM^{-1} \cdot cm^{-1}$ (48), respectively, and were cross-checked with Bradford assay using their molecular weights of 32.6 (11) and 45.8 kDa (49).

The reduction of ferricyt *c* by $O_2^{\bullet-}$ generated from X/XO was followed spectrophotometrically at 550 nm, using a $\Delta\varepsilon_{550nm} = 21$ $mM^{-1} \cdot cm^{-1}$ (50), both in the absence and in the presence of various concentrations of Cygb or Cu,Zn-SOD. Kinetic and spectral measurements were performed on an Agilent 8453 diode–array spectrophotometer (Palo Alto). The reaction was performed in a total volume of 800 μL containing 50 μM ferricyt *c*, 50 μM X, 0.1 mM EDTA, and 50 mM air-equilibrated phosphate buffer (pH 7.8) at room temperature and initiated by adding XO, the final concentration being 70 nM. Of note, preliminary experiments in the presence or absence of catalase 400 U/mL gave identical results for these measurements of initial rate, so catalase was not included in subsequent assays.

For EPR spin-trapping measurements of $O_2^{\bullet-}$ and SOD activity, EPR spectra were recorded at X-band on a Bruker EMX spectrometer with HS resonator at RT. A series of 25 sequential scans were performed over ∼18 min to monitor accumulation of the $O_2^{\bullet-}$ spin trap adduct. The rate of $O_2^{\bullet-}$ adduct accumulation was determined from the linear phase of this reaction (∼0 to 420 s), with the rate of change in concentration in nanomolar/minute calculated by double integration of the spectra relative to 4-oxo-TEMPO standards of known concentration. Instrument parameters were the following (51): microwave frequency, 9.78 GHz; microwave power, 20 mW; modulation frequency, 100 kHz; modulation amplitude, 0.5 G; time constant, 164 ms; and scan time, 42 s. For each reaction, 0.1 μM XO and 300 μM X were used with 10 mM spin trap, DIPPMPO. Reactions were performed in PBS (10 mM phosphate, 138 mM NaCl, and 2.7 mM KCl), and 0.1 mM EDTA, pH 7.4, that was passed through Chelex resin to remove any free metal ions. Reactions were initiated by addition of X and samples quickly loaded into an EPR flat cell that was then placed in the resonator of the EPR instrument.

Cyanide-bound ferric Cygb, CN-Fe^{3+}Cygb (CN-Cygb) was made by treating ferric Cygb (80 μL of ∼1.2 mM protein) with an excess of NaCN, incubating on ice for 30 min, and running down Sephadex G-25 to remove excess CN. CO-Fe^{2+}Cygb (CO-Cygb) was prepared by reductive titration of Cygb with dithionite in CO-saturated buffer. Care was taken to use only enough dithionite to reach complete reduction of the Cygb and formation of CO-Cygb monitored by its absorbance at 420 nM.

Stopped-Flow Measurements of the Rate of $O_2^{\bullet-}$ Dismutation. These assays were carried out in 100 mM Hepes and 0.1 mM EDTA, pH 7.8, that were passed through Chelex resin. The KO_2 stock solutions were made in anhydrous dimethyl sulfoxide (DMSO) dried over molecular sieves as described (15) with some modifications and handled under a continuous stream of dry N_2 gas. Approximately 0.1 g of KO_2 was mixed with 25 mL of dry DMSO in a septum-sealed 50-mL tube that had been flushed with dry N_2 gas and thoroughly mixed, resulting in a stock solution of ∼2 mM $O_2^{\bullet-}$. The 1-mL syringes used for the KO_2/DMSO solution were filled from the 50-mL tube through the septum seal and immediately mounted on the stopped-flow instrument. An Applied Photophysics SX20 Stopped-Flow Spectrometer was used to measure the catalytic decay of $O_2^{\bullet-}$ by Cygb, Cu,Zn-SOD, and Mn-SOD in aqueous buffer. The system was configured for asymmetric mixing at a volume ratio of 25:1 and the shot volume adjusted to ∼300 μL. The rate of $O_2^{\bullet-}$ decay for each protein

concentration tested was measured at least five times at RT, and the average rate (k_{obs}) was plotted against protein concentration to estimate the second-order rate constant.

Spectrophotometric Measurements of the Reaction of Cygb with $O_2^{\bullet-}$. Anaerobic titrations of ferric Cygb were carried out in 100 mM Hepes and 0.1 mM EDTA, pH 7.8, that was passed through Chelex resin. Ferric Cygb, at a concentration of ~10 μM, was made anaerobic in a sealed tonometer fitted with a 1-cm cuvette by repeated steps of evacuation with house vacuum followed by flushing with argon gas using a two-sided manifold and two-position stopcock. The KO_2 stock solutions were made in anhydrous DMSO as described above (*Stopped-Flow Measurements of the Rate of $O_2^{\bullet-}$ Dismutation*) and handled under a continuous stream of dry N_2 gas. Sodium dithionite was dissolved in buffer made anaerobic by continuous flushing with argon gas. Ferric Cygb was titrated in the anaerobic tonometer with these solutions using a long-needled, gas-tight titration syringe introduced through the septum seal of the tonometer. Optical spectra of 0.5 s were recorded, using an Agilent 8453 diode–array spectrophotometer, ~4 s after addition and mixing of the reactant. For detecting the spectrum of $CygbFe^{2+}$-CO, the anaerobic tonometer containing the protein solution was flushed with pure CO until the solution was saturated. A 1-mL aliquot of the KO_2 solution was also flushed in the same way just prior to use. All titration experiments were done at RT. Measurements of the reaction of $CygbFe^{3+}$ and $CygbFe^{2+}$-O_2 with 10 μM Cygb were performed with stoichiometric 1:1 additions of $KO_2 \times 3$ and spectra measured every 0.5 s within 4 s of addition and mixing

To assay the formation of the low levels of $CygbFe^{2+}$-O_2 formed from $CygbFe^{3+}$ under conditions of sustained $O_2^{\bullet-}$ generation, the XO/X-generating system was used. First, measurements of the difference spectra were performed using a Cary 300 dual-beam spectrophotometer. Then, time-dependent measurements of the increase in absorption at the 578-nM peak of $CygbFe^{2+}$-O_2 relative to the isosbestic point at 600 nm were measured every 0.5 s for 1,200 s following the addition of X to start the reaction.

Human Aortic SMC Studies. Clonetics human aortic SMCs (CC-2571) and culture medium were from Lonza. Cells were maintained at 37 °C in a humidified CO_2 atmosphere and passaged at less than 80% confluency. Experiments used exponentially growing cells in passages five to seven. SMCs were trypsinized, counted, and 2×10^6/mL were incubated with the X/XO $O_2^{\bullet-}$-generating system (X 300 μM and XO 0.1 μM) with or without added Cygb. The reactions were carried out in 400 μL of PBS buffer and 0.1 mM EDTA, pH 7.4. EPR spin-trapping was performed using 10 mM DIPPMPO. In parallel experiments, in the absence of the spin trap, cell viability was measured with trypan blue, 0.02% final concentration, at 5, 15, and 30 min postinitiating $O_2^{\bullet-}$ generation. Cell counts were performed in a hemocytometer using a light microscope.

Gene KD Experiments. Human aortic SMCs were transfected with Cygb siRNA (Santa Cruz Biotechnology) using Lipofectamine RNAiMAX (Invitrogen) per the manufacturer's recommendations. Approximately 1×10^6 cells at ~80% confluency in one well (~9.5 cm^2) of a 6-well culture plate were transfected. Lipofectamine RNAiMAX was diluted in Opti-MEM (minimal essential medium) (10 μL:150 μL). Cygb siRNA (2.5 μL of 10 μM) or Scr siRNA was diluted in 150 μL Opti-MEM. Diluted Lipofectamine RNAiMAX and diluted siRNA or Scr siRNA were mixed, incubated at RT for 5 minutes, and added to cells. Cells were incubated at 37 °C in a 5% CO_2-humidified incubator for 7 h and then switched to complete growth medium. At 48 h posttransfection, the Cygb- or the Scr siRNA–transfected cells were collected for studies and Cygb expression evaluated by quantitative Western blotting against known amounts of purified rh-Cygb.

Human Scr siRNA–treated SMCs or Cygb siRNA–treated SMCs were trypsinized, counted, and 1×10^6/mL were incubated with 50 μM menadione in the presence of the spin trap DMPO (50 mM) in 400 μL of PBS buffer and 0.1 mM EDTA, pH 7.4. Cygb siRNA–treated cells were also treated with SOD_m (50 μM M40403) (17) and rh-Cygb (2.5 μM or 0.5 μM). EPR data were collected and quantitated as described in *Measurements of SOD Activity*. Parallel cell viability measurements were performed in the absence of the spin trap just prior to and 30 min after menadione treatment using trypan blue.

Measurements of $O_2^{\bullet-}$ Generation in Vessels of WT and *Cygb*$^{-/-}$ Mice. DHE-derived fluorescence was used to measure $O_2^{\bullet-}$ generation in aortic vessels. Aortas were harvested from C57BL/6 (WT) or *Cygb*$^{-/-}$ (Cygb-KO) mice frozen in optimal cutting temperature compound (Tissue-Tek, Sakura Finetek, Inc.), cryosectioned to 5-μm sections. Aortic sections were incubated with DHE alone (Molecular Probes, Inc.) or together with 10 μM menadione in the presence or absence of 100 μM SOD_m (GC4419, Galera Therapeutics) (21) in the dark for 30 min. The slides were rinsed with PBS, mounted in antifade mounting media Fluoromount-G (Southern Biotechnology), cover slipped, then imaged at 40× using a confocal microscope (Olympus FV3000). The fluorescence intensity was analyzed using microscope-provided software. The C57BL/6 male mice used were purchased from Jackson Laboratory, and the *Cygb*$^{-/-}$ mice were derived from breeding pairs provided by Norifumi Kawada, Osaka City University, Osaka, Japan.

Statistical Analysis. Values are expressed as the mean ± SEM, unless noted otherwise, of at least three repeated measurements. Statistical significance of difference was evaluated by Student's *t* test, with $P < 0.05$ considered statistically significant.

Data Availability. All study data are included in the article and/or *SI Appendix*. SigmaPlot 13 and GraphPad Prism files for plotted data and image files and PowerPoint files for gel images have been deposited in figshare:

Fig. 1 entry (DOI: 10.6084/m9.figshare.14802927); Fig. 2 entry (DOI: 10.6084/m9.figshare.16918909); Fig. 3 entry (DOI: 10.6084/m9.figshare.16918969); Fig. 4 entry (DOI: 10.6084/m9.figshare.16919011); Fig. 5 entry (DOI: 10.6084/m9.figshare.16919014); Fig. 6 entry (DOI: 10.6084/m9.figshare.16919026); Fig. 7 entry (DOI: 10.6084/m9.figshare.16919047); Fig. 8 entry (DOI: 10.6084/m9.figshare.16919068); Fig. 9 entry (DOI: 10.6084/m9.figshare.16919074); Fig. 10 entry (DOI: 10.6084/m9.figshare.16919086); *SI Appendix*, Figs. S1–S3 entry (DOI: 10.6084/m9.figshare.16919182).

ACKNOWLEDGMENTS. This work was supported by NIH/National Heart, Lung, and Blood Institute grants R01HL131941 and R01HL135648. We thank Dr. Liwen Zhang of The Ohio State University Campus Chemical Instrument Center Proteomics Core for technical support. We also thank Dr. Norifumi Kawada for his encouragement and providing the *Cygb*$^{-/-}$ breeding pairs used to derive the mice for the aortic assays. We are grateful to Dr. John S. Olson and Dr. Irwin Fridovich for their advice and helpful comments on this work over the years leading to this manuscript.

1. T. Burmester, B. Ebner, B. Weich, T. Hankeln, Cytoglobin: A novel globin type ubiquitously expressed in vertebrate tissues. *Mol. Biol. Evol.* **19**, 416–421 (2002).
2. N. Kawada *et al.*, Characterization of a stellate cell activation-associated protein (STAP) with peroxidase activity found in rat hepatic stellate cells. *J. Biol. Chem.* **276**, 25318–25323 (2001).
3. J. T. Trent III, M. S. Hargrove, A ubiquitously expressed human hexacoordinate hemoglobin. *J. Biol. Chem.* **277**, 19538–19545 (2002).
4. T. Hankeln *et al.*, Neuroglobin and cytoglobin in search of their role in the vertebrate globin family. *J. Inorg. Biochem.* **99**, 110–119 (2005).
5. B. J. Smagghe, J. T. Trent III, M. S. Hargrove, NO dioxygenase activity in hemoglobins is ubiquitous in vitro, but limited by reduction in vivo. *PLoS One* **3**, e2039 (2008).
6. A. M. Gardner, M. R. Cook, P. R. Gardner, Nitric-oxide dioxygenase function of human cytoglobin with cellular reductants and in rat hepatocytes. *J. Biol. Chem.* **285**, 23850–23857 (2010).
7. A. Fago, C. Hundahl, H. Malte, R. E. Weber, Functional properties of neuroglobin and cytoglobin. Insights into the ancestral physiological roles of globins. *IUBMB Life* **56**, 689–696 (2004).
8. F. E. McRonald, J. M. Risk, N. J. Hodges, Protection from intracellular oxidative stress by cytoglobin in normal and cancerous oesophageal cells. *PLoS One* **7**, e30587 (2012).
9. D. Li *et al.*, Cytoglobin up-regulated by hydrogen peroxide plays a protective role in oxidative stress. *Neurochem. Res.* **32**, 1375–1380 (2007).
10. N. J. Hodges, N. Innocent, S. Dhanda, M. Graham, Cellular protection from oxidative DNA damage by over-expression of the novel globin cytoglobin in vitro. *Mutagenesis* **23**, 293–298 (2008).
11. J. Butler, W. H. Koppenol, E. Margoliash, Kinetics and mechanism of the reduction of ferricytochrome c by the superoxide anion. *J. Biol. Chem.* **257**, 10747–10750 (1982).
12. S. Goldstein, I. Fridovich, G. Czapski, Kinetic properties of Cu,Zn-superoxide dismutase as a function of metal content–Order restored. *Free Radic. Biol. Med.* **41**, 937–941 (2006).
13. C. Frejaville *et al.*, 5-diethoxyphosphoryl-5-methyl-1-pyrroline N-oxide (Depmpo) – A new phosphorylated nitrone for the efficient in-vitro and in-vivo spin-trapping of oxygen-centered radicals. *J. Chem. Soc. Chem. Commun.* (15), 1793–1794 (1994).
14. F. Chalier, P. Tordo, 5-Diisopropoxyphosphoryl-5-methyl-1-pyrroline N-oxide, DIPPMPO, a crystalline analog of the nitrone DEPMPO: Synthesis and spin trapping properties. *J Chem Soc Perk T* **2**, 2110–2117 (2002).
15. D. P. Riley, W. J. Rivers, R. H. Weiss, Stopped-flow kinetic analysis for monitoring superoxide decay in aqueous systems. *Anal. Biochem.* **196**, 344–349 (1991).
16. X. Liu *et al.*, Cytoglobin regulates blood pressure and vascular tone through nitric oxide metabolism in the vascular wall. *Nat. Commun.* **8**, 14807 (2017).
17. D. Salvemini *et al.*, A nonpeptidyl mimic of superoxide dismutase with therapeutic activity in rats. *Science* **286**, 304–306 (1999).
18. J. L. Zweier, G. Ilangovan, Regulation of nitric oxide metabolism and vascular tone by cytoglobin. *Antioxid. Redox Signal.* **32**, 1172–1187 (2020).

19. M. A. El-Mahdy *et al.*, Chronic cigarette smoke exposure triggers a vicious cycle of leukocyte and endothelial-mediated oxidant stress that results in vascular dysfunction. *Am. J. Physiol. Heart Circ. Physiol.* **319**, H51–H65 (2020).
20. M. A. El-Mahdy *et al.*, Long-term electronic cigarette exposure induces cardiovascular dysfunction similar to tobacco cigarettes: Role of nicotine and exposure duration. *Am. J. Physiol. Heart Circ. Physiol.* **320**, H2112–H2129 (2021).
21. M. A. El-Mahdy *et al.*, The novel SOD mimetic GC4419 increases cancer cell killing with sensitization to ionizing radiation while protecting normal cells. *Free Radic. Biol. Med.* **160**, 630–642 (2020).
22. X. Liu *et al.*, Characterization of the function of cytoglobin as an oxygen-dependent regulator of nitric oxide concentration. *Biochemistry* **51**, 5072–5082 (2012).
23. H. Li, C. Hemann, T. M. Abdelghany, M. A. El-Mahdy, J. L. Zweier, Characterization of the mechanism and magnitude of cytoglobin-mediated nitrite reduction and nitric oxide generation under anaerobic conditions. *J. Biol. Chem.* **287**, 36623–36633 (2012).
24. J. Wen *et al.*, Protective effects of recombinant human cytoglobin against chronic alcohol-induced liver disease in vivo and in vitro. *Sci. Rep.* **7**, 41647 (2017).
25. L. Ou *et al.*, Recombinant human cytoglobin prevents atherosclerosis by regulating lipid metabolism and oxidative stress. *J. Cardiovasc. Pharmacol. Ther.* **23**, 162–173 (2018).
26. Y. Fujita *et al.*, Melanoma transition is frequently accompanied by a loss of cytoglobin expression in melanocytes: A novel expression site of cytoglobin. *PLoS One* **9**, e94772 (2014).
27. F. Trandafir *et al.*, Neuroglobin and cytoglobin as potential enzyme or substrate. *Gene* **398**, 103–113 (2007).
28. Y. Li *et al.*, Validation of lucigenin (bis-N-methylacridinium) as a chemilumigenic probe for detecting superoxide anion radical production by enzymatic and cellular systems. *J. Biol. Chem.* **273**, 2015–2023 (1998).
29. S. I. Liochev, I. Fridovich, Lucigenin (bis-N-methylacridinium) as a mediator of superoxide anion production. *Arch. Biochem. Biophys.* **337**, 115–120 (1997).
30. S. Hanai *et al.*, Roles of N- and C-terminal domains in the ligand-binding properties of cytoglobin. *J. Inorg. Biochem.* **179**, 1–9 (2018).
31. H. Maeda *et al.*, Design of a practical fluorescent probe for superoxide based on protection-deprotection chemistry of fluoresceins with benzenesulfonyl protecting groups. *Chemistry* **13**, 1946–1954 (2007).
32. D. Klug-Roth, I. Fridovich, J. Rabani, Pulse radiolytic investigations of superoxide catalyzed disproportionation. Mechanism for bovine superoxide dismutase. *J. Am. Chem. Soc.* **95**, 2786–2790 (1973).
33. B. Gray, A. J. Carmichael, Kinetics of superoxide scavenging by dismutase enzymes and manganese mimics determined by electron spin resonance. *Biochem. J.* **281**, 795–802 (1992).
34. H. J. Forman, I. Fridovich, Superoxide dismutase: A comparison of rate constants. *Arch. Biochem. Biophys.* **158**, 396–400 (1973).
35. H. C. Sutton, P. B. Roberts, C. C. Winterbourn, The rate of reaction of superoxide radical ion with oxyhaemoglobin and methaemoglobin. *Biochem. J.* **155**, 503–510 (1976).
36. H. Sugimoto *et al.*, Structural basis of human cytoglobin for ligand binding. *J. Mol. Biol.* **339**, 873–885 (2004).
37. H. Sawai *et al.*, Characterization of the heme environmental structure of cytoglobin, a fourth globin in humans. *Biochemistry* **42**, 5133–5142 (2003).
38. W. F. Alzawahra, M. A. Talukder, X. Liu, A. Samouilov, J. L. Zweier, Heme proteins mediate the conversion of nitrite to nitric oxide in the vascular wall. *Am. J. Physiol. Heart Circ. Physiol.* **295**, H499–H508 (2008).
39. T. T. Thuy *et al.*, Absence of cytoglobin promotes multiple organ abnormalities in aged mice. *Sci. Rep.* **6**, 24990 (2016).
40. M. B. Amdahl, C. E. Sparacino-Watkins, P. Corti, M. T. Gladwin, J. Tejero, Efficient reduction of vertebrate cytoglobins by the cytochrome b_5/cytochrome b_5 reductase/NADH system. *Biochemistry* **56**, 3993–4004 (2017).
41. R. C. Bray *et al.*, Reduction and inactivation of superoxide dismutase by hydrogen peroxide. *Biochem. J.* **139**, 43–48 (1974).
42. A. E. Dikalova *et al.*, Sirt3 impairment and SOD2 hyperacetylation in vascular oxidative stress and hypertension. *Circ. Res.* **121**, 564–574 (2017).
43. L. A. MacMillan-Crow, J. P. Crow, J. D. Kerby, J. S. Beckman, J. A. Thompson, Nitration and inactivation of manganese superoxide dismutase in chronic rejection of human renal allografts. *Proc. Natl. Acad. Sci. U.S.A.* **93**, 11853–11858 (1996).
44. B. van der Loo *et al.*, Enhanced peroxynitrite formation is associated with vascular aging. *J. Exp. Med.* **192**, 1731–1744 (2000).
45. J. Tejero *et al.*, Peroxidase activation of cytoglobin by anionic phospholipids: Mechanisms and consequences. *Biochim. Biophys. Acta* **1861**, 391–401 (2016).
46. V. Massey, P. E. Brumby, H. Komai, Studies on milk xanthine oxidase. Some spectral and kinetic properties. *J. Biol. Chem.* **244**, 1682–1691 (1969).
47. E. Margoliash, N. Frohwirt, Spectrum of horse-heart cytochrome c. *Biochem. J.* **71**, 570–572 (1959).
48. J. W. Whittaker, M. M. Whittaker, Active-site spectral studies on manganese superoxide-dismutase. *J. Am. Chem. Soc.* **113**, 5528–5540 (1991).
49. W. F. Beyer Jr., J. A. Reynolds, I. Fridovich, Differences between the manganese- and the iron-containing superoxide dismutases of *Escherichia coli* detected through sedimentation equilibrium, hydrodynamic, and spectroscopic studies. *Biochemistry* **28**, 4403–4409 (1989).
50. B. van Gelder, E. C. Slater, The extinction coefficient of cytochrome c. *Biochim. Biophys. Acta* **58**, 593–595 (1962).
51. V. Roubaud, S. Sankarapandi, P. Kuppusamy, P. Tordo, J. L. Zweier, Quantitative measurement of superoxide generation and oxygen consumption from leukocytes using electron paramagnetic resonance spectroscopy. *Anal. Biochem.* **257**, 210–217 (1998).